Imaginary-Stark skin effect

Heng Lin [1], Jinghui Pi [1,*], Yunyao Qi [1], Wei Qin [2], Franco Nori [3,4] and Gui-Lu Long [1,5,6,†]

[1] State Key Laboratory of Low-Dimensional Quantum Physics and Department of Physics, Tsinghua University, Beijing 100084, China

[2] Center for Joint Quantum Studies and Department of Physics, Tianjin University, Tianjin 300350, China

[3] Center for Quantum Computing, RIKEN, Wako-shi, Saitama 351-0198, Japan

[4] Department of Physics, The University of Michigan, Ann Arbor, Michigan 48109-1040, USA

[5] Frontier Science Center for Quantum Information, Beijing 100084, China

[6] Beijing Academy of Quantum Information Sciences, Beijing 100193, China

(Received 1 May 2024; accepted 10 July 2025; published 13 August 2025)

A unique phenomenon in non-Hermitian systems is the non-Hermitian skin effect (NHSE), namely, the boundary localization of continuous-spectrum eigenstates. However, studies on the NHSE in systems without translational invariance are still limited. Here, we unveil a new class of NHSE, dubbed the imaginary-Stark skin effect (ISSE), in a one-dimensional lossy lattice with a spatially increasing loss rate. This ISSE is beyond the framework of non-Bloch band theory and exhibits intriguing properties significantly different from the conventional NHSE. Specifically, the energy spectrum of our model has a T-shaped feature, with approximately half of the eigenstates localized at the left boundary. Furthermore, each skin mode can be expressed as a single stable, exponentially decaying wave within the bulk region. Such peculiar behaviors are analyzed via the transfer-matrix method, whose eigendecomposition quantifies the formation of the ISSE. Our work provides new insights into the NHSE in systems without translational symmetry and contributes to the understanding of non-Hermitian systems.

DOI: 10.1103/xc42-7hcg

I. INTRODUCTION

In closed systems, the Hermiticity of Hamiltonians is a fundamental postulate. In contrast, for open systems, non-Hermiticity emerges and can be described by effective Hamiltonians [1], displaying peculiar properties and potential applications in various fields [2–24]. A unique feature of non-Hermitian systems is the non-Hermitian skin effect (NHSE), namely, the boundary localization of bulk band eigenstates, causing a high sensitivity of the spectrum to the boundary conditions [25–27]. The NHSE can induce phenomena without Hermitian counterparts, including unidirectional physical effects [28–30], critical phenomena [31–34], and geometry-related effects in high dimensions [35–39]. Notably, the NHSE has also been observed across diverse experimental platforms, such as active mechanical materials [40–42], electrical circuits [43–45], optical systems [46–49], and cold atoms [50].

Thus far, most studies of the NHSE focus on translation-invariant systems, amenable to non-Bloch band theory [26,51–53]. Specifically, the extended Bloch waves are replaced by exponentially decaying waves, drastically changing the system topology and thus reshaping the conventional bulk-boundary correspondence [54–66]. Recently, studies on the NHSE have also been extended to translational symmetry-breaking systems, mainly including quasicrystals [67–73], and systems with disorder [74–81] or single impurity [34,82,83]. In a system with a single impurity, the translational symmetry is preserved outside the impurity, and thus, the exponentially decaying wave ansatz of non-Bloch theory still holds. For quasicrystals and disordered systems, the NHSE is typically quantified by the inverse participation ratio, which offers only a superficial description of the NHSE and fails to analyze the wave function comprehensively. Therefore, it remains unclear whether the skin modes in transnational symmetry-breaking systems can exhibit distinct properties, compared to those in translation-invariant systems. Furthermore, the accurate quantification of the NHSE is also unsolved when non-Bloch band theory breaks down.

Here, we present a new class of NHSE, i.e., the imaginary-Stark skin effect (ISSE), which is beyond the framework of non-Bloch band theory. The ISSE demonstrates a distinct behavior compared to the NHSE in translation-invariant systems, and can be studied by the asymptotic and convergence properties of the transfer-matrix eigenvalues. This fills an existing gap in the research on NHSE in translational symmetry-breaking systems. We consider a one-dimensional lossy lattice with a unidirectionally increasing loss rate. This scenario resembles a lattice subjected to a leftward imaginary field, and the energy spectrum of such a system displays a T-shaped feature [84], with its upper-half eigenstates localized at the left boundary. Surprisingly, these skin modes exhibit an almost uniform decay rate within the bulk region, despite the broken translational invariance. Moreover, our numerical results indicate that these skin modes can be approximately

*Contact author: pijh14@gmail.com

†Contact author: gllong@tsinghua.edu.cn

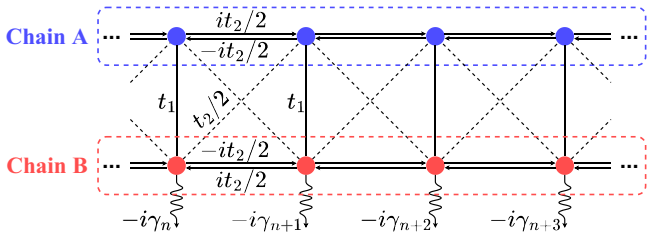

FIG. 1. A schematic diagram of the non-Hermitian lattice. The Hermitian interaction is characterized by the hopping parameters t_1 and t_2, while the monotonically increasing dissipation γ_n features the non-Hermitian processes. Here, n labels the lattice index.

expressed as a *single* wave within the bulk region. Therefore, the ISSE fundamentally differs from the conventional NHSE described by non-Bloch band theory (e.g., bipolar [85], corner [65,86], and geometry-dependent skin effect [36]), where each skin mode comprises *two* exponentially decaying waves with an identical decay rate. We employ the transfer-matrix method to establish a connection between the ISSE and the convergence rate of the eigenvalues of the transfer matrix. The wave function is divided into two parts based on the eigendecomposition of the transfer matrix, with one part dominating the behavior of the skin modes in the bulk, accounting for the peculiar behavior of the ISSE.

II. MODEL OF THE IMAGINARY-STARK SKIN EFFECT

We consider a single particle in a one-dimensional lossy lattice (see Fig. 1), which can be divided into two chains, labeled A and B. We define $|n, A(B)\rangle$ as a basis state, where the particle is in the nth site of chain A(B). The projection of the wave function $|\psi\rangle$ is denoted as $\psi_n^{A(B)} = \langle n, A(B)|\psi\rangle$ and $\psi = (\psi_1^A, \psi_1^B, \psi_2^A, \psi_2^B, \dots)$. Then, the eigenequations of this model can be expressed as

$$\begin{aligned} E\psi_n^A &= t_1\psi_n^B + \frac{t_2}{2}\left(\psi_{n-1}^B + \psi_{n+1}^B\right) + i\frac{t_2}{2}\left(\psi_{n-1}^A - \psi_{n+1}^A\right), \\ E\psi_n^B &= t_1\psi_n^A + \frac{t_2}{2}\left(\psi_{n-1}^A + \psi_{n+1}^A\right) - i\frac{t_2}{2}\left(\psi_{n-1}^B - \psi_{n+1}^B\right) \\ &\quad - i\gamma_n\psi_n^B, \end{aligned} \tag{1}$$

where t_1 and t_2 are the hopping parameters, and γ_n represents the loss rate at the nth site of chain B. When γ_n is uniform, this model can be transformed into the non-Hermitian Su-Schrieffer-Heeger model with asymmetric hopping, whose NHSE has been studied [26]. This manuscript focuses on the case where γ_n monotonically increases and diverges as n approaches infinity. The energy spectrum of such a model demonstrates a T-shaped feature, as shown in Figs. 2(a)–2(d). Furthermore, the eigenstates in the "−" horizontal part of the T-shaped spectrum display a marked distinction from those in the "|" vertical part. Specifically, the eigenstates in the "−" part localize at the left boundary, manifesting the NHSE. This is consistent with the fact that the "−" part of the periodic-boundary-condition (PBC) spectrum encircles the corresponding open-boundary-condition (OBC) spectrum [52,87], as shown in the insets of Figs. 2(a)–2(d). Conversely, the eigenstates in the "|" part are localized around each site of chain B within the bulk region [see Fig. 2(e)]. Notably, the eigenstates in the "−" part predominantly reside in chain A [see Fig. 2(f)], while those in the "|" part in chain B [see

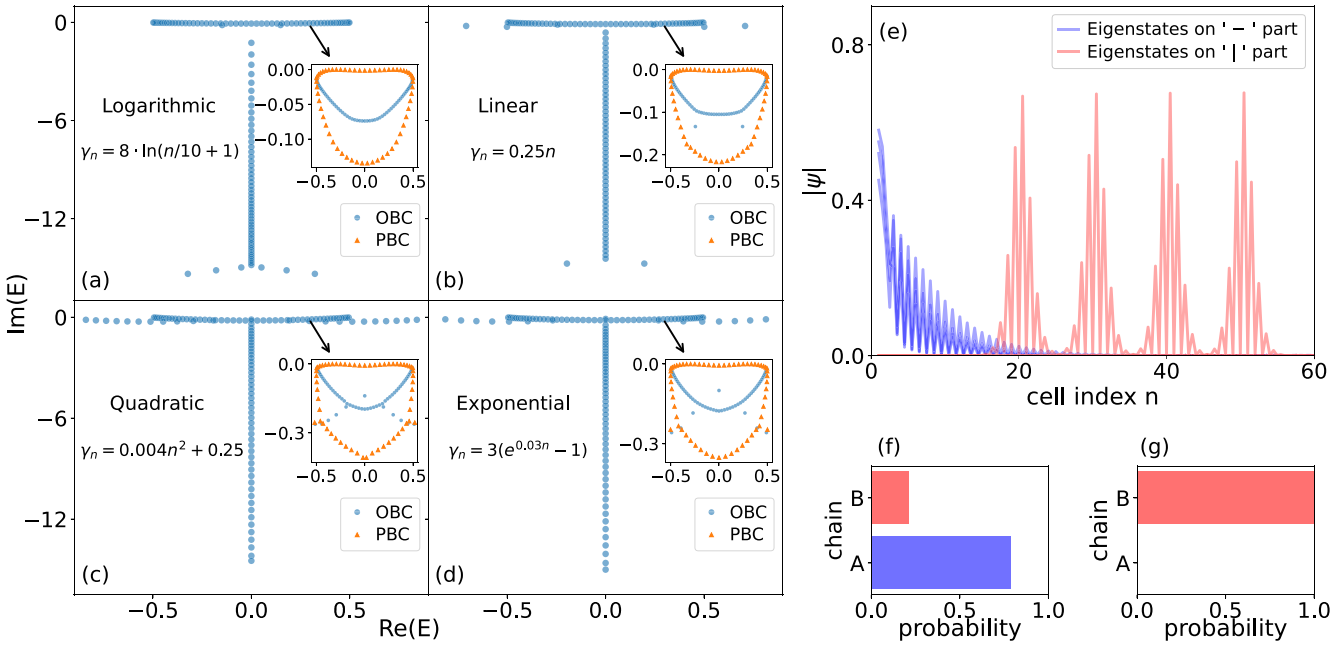

FIG. 2. (a)–(d) Energy spectra for various loss rate functions γ_n. Insets refer to the "−" horizontal parts of the T-shaped spectra. (e) Profiles of the eigenstates from the "−" and "|" parts of the T-shaped spectrum. Eight eigenstates are displayed, of which four are in the "−" part and the other four are in the "|" vertical part. (f), (g) Average probabilities $\Sigma_n|\psi_n^S|^2$ of a particle in chains A and B, where $S \in \{A, B\}$, and this summation is averaged over eigenstates in either the "−" (f) or "|" (g) part of the T-shaped spectrum. In panels (e)–(g), $\gamma_n = 0.25n$, and in panels (a)–(g), $t_1 = 0.4$, $t_2 = 0.5$, and the chain length $L = 60$.

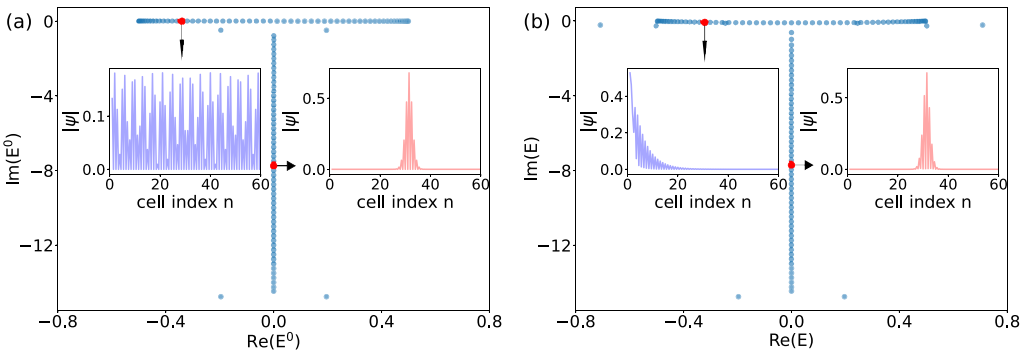

FIG. 3. Energy spectra for turning "off" (a) and "on" (b) the coupling between chains A and B. Insets are the profiles of typical eigenstates from the "−" and "|" parts of the spectra, corresponding to the red points. The parameters are $t_1 = 0.4$, $t_2 = 0.5$, $\gamma_n = 0.25n$, and $L = 60$.

Fig. 2(g)]. This implies that chains A and B are relatively independent. This distinction between chains A and B is also reflected in their dynamical behavior, and a detailed analysis of this is provided in Appendix A.

To gain insights, we turn off the coupling between chains A and B, making them independent. Hereafter, we use E^0 and E to denote the energies when chains A and B are decoupled and coupled, respectively. The energy of chain A is real and given by $E^{0,-} = t_2 \sin(k)$, whose eigenstates are extended standing waves with Bloch wave vector k. In chain B, each site is linked to an eigenstate localized around it, with the energy closely approximated by its imaginary potential. This is similar to the Wannier-Stark localization [88,89]. The superposition of the spectra of chains A and B results in a T-shaped spectrum, and the "−" and "|" parts are formed, as depicted in Fig. 3(a), by the energies of chains A and B, respectively. Upon introducing the coupling between chains A and B, the spectrum undergoes certain distortions, but retains, almost unchanged, the T shape [see Fig. 3(b)]. In such a coupled case, the eigenstates corresponding to the "|' part are still localized around their respective sites in chain B. However, the NHSE appears in the eigenstates of the "−" part.

III. FEATURES OF THE IMAGINARY-STARK SKIN EFFECT

For simplicity, we apply a local unitary transformation to the basis $|n, A(B)\rangle$ and then obtain a new basis $|n, A'(B')\rangle$. Specifically, we define $|n, A'\rangle = (|n, A\rangle - i|n, B\rangle)/\sqrt{2}$ and $|n, B'\rangle = (|n, A\rangle + i|n, B\rangle)/\sqrt{2}$. Consequently, the eigenequations [Eq. (1)] become more concise, yielding (see Appendix B for details)

$$\begin{aligned} E\psi_n^{A'} &= -i\frac{\gamma_n}{2}\psi_n^{A'} + t_2\psi_{n-1}^{B'} + \left(t_1 + \frac{\gamma_n}{2}\right)\psi_n^{B'}, \\ E\psi_n^{B'} &= -i\frac{\gamma_n}{2}\psi_n^{B'} + \left(t_1 - \frac{\gamma_n}{2}\right)\psi_n^{A'} + t_2\psi_{n+1}^{A'}, \end{aligned} \tag{2}$$

where $\psi_n^{A'(B')} = \langle n, A'(B')|\psi\rangle$ is the wave function projected onto $|n, A'(B')\rangle$. We use H' to denote the Hamiltonian after this transformation.

The ISSE exhibits two features. First, although the loss rate γ_n increases spatially in the lattice, the skin modes have an almost uniform decay rate within the bulk region. This is illustrated by the linearity of the wave function $\psi_n^{A'(B')}$ on a logarithmic scale [see Fig. 4(b)]. Second, for one-dimensional spatially periodic tight-binding non-Hermitian models, the eigenstates can be written as a superposition of two exponentially decaying waves. Under the OBCs, constructing continuum bands requires the amplitudes of these two waves to be equal [26,51–53], inducing interference in the bulk [see Fig. 4(a)]. However, in our model, numerical results show the absence of interference. This indicates that each skin mode can be approximately expressed as a single exponentially decaying wave within the bulk region [see Fig. 4(b)], i.e.,

$$\psi_n^{S'} \sim \beta^n, \tag{3}$$

where $S' \in \{A', B'\}$ and $\beta < 1$ is a uniform decay rate. This result differs greatly from the spatially periodic cases.

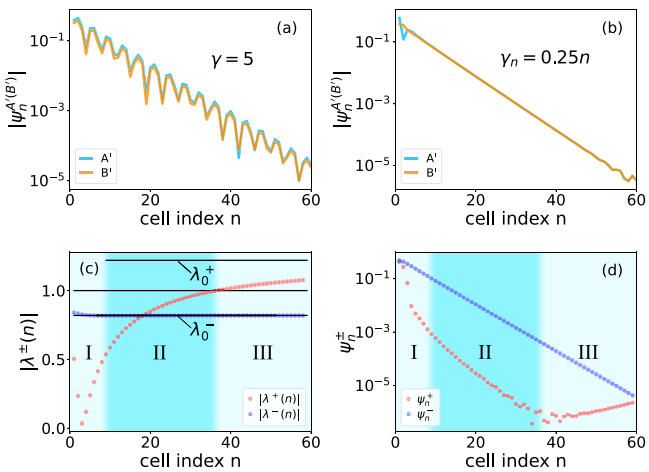

FIG. 4. (a), (b) Profiles of the eigenstates for uniform and linear loss rates. For a uniform loss rate, two exponentially decaying waves interfere in the bulk. Conversely, the linear loss case only exhibits a dominant exponentially decaying and no interference. (c) Modulus of the eigenvalues of the transfer matrix, $|\lambda^{\pm}(n)|$, vs n. The horizontal black lines from top to bottom are λ_0^+, 1, and λ_0^-, respectively. (d) Decomposition components of the wave function, $\psi_n^{\pm}$, vs n. The parameters are $t_1 = 0.4$, $t_2 = 0.5$, $L = 60$ in all plots, while $\gamma = 5$ in panel (a) and $\gamma_n = 0.25n$ in panels (b)–(d).

Let us first adopt a rough approach to obtain β in Eq. (3). We define the ratio $\beta_n = \psi_n^{S'}/\psi_{n-1}^{S'}$, and substitute β_n into the bulk eigenequation in Eq. (2), yielding

$$0 = \gamma_n\left[iE - \frac{t_2}{2}\left(\beta_{n+1} - \beta_n^{-1}\right)\right] + E^2 - \left(t_1 + t_2\beta_n^{-1}\right)(t_1 + t_2\beta_{n+1}). \tag{4}$$

To obtain solutions $\beta_n \approx \beta$ consistent with our numerical findings in Eq. (3) and also to ensure this equation holds for arbitrary n, the γ_n term must be approximately zero, that is,

$$iE - \frac{t_2}{2}\left(\beta_{n+1} - \beta_n^{-1}\right) \approx 0, \tag{5}$$

which gives two solutions of β:

$$\beta_\pm \approx \frac{iE}{t_2}[1 \pm \sqrt{1 - (t_2/E)^2}]. \tag{6}$$

Our simulation indicates that the analytical solution β_- agrees with the numerical results of β.

IV. ANALYSIS OF THE IMAGINARY-STARK SKIN EFFECT

A. Transfer-matrix method

The above approach fails to explain why β_-, instead of β_+, fits β and how the ISSE arises. Below, we analyze the model more accurately using the transfer-matrix method [90–92]. Consider the projected bulk eigenequations in a subspace spanned by the bases $|n-1, B'\rangle$ and $|n, A'\rangle$:

$$\begin{aligned}\langle n-1, B'|H'|\psi\rangle &= E\langle n-1, B'|\psi\rangle,\\ \langle n, A'|H'|\psi\rangle &= E\langle n, A'|\psi\rangle,\end{aligned} \tag{7}$$

which can be expressed as

$$\begin{pmatrix} M_{n,0} & M_{n,1}\end{pmatrix}\begin{pmatrix}|\psi(n-1)\rangle\\ |\psi(n)\rangle\end{pmatrix} = 0, \tag{8}$$

where $|\psi(n)\rangle = (\psi_n^{A'},\ \psi_n^{B'})^{\mathcal{T}}$ is the wave function on the nth unit cell, and

$$\begin{aligned} M_{n,0} &= \begin{pmatrix} t_1 - \frac{\gamma_{n-1}}{2} & -i\frac{\gamma_{n-1}}{2} - E\\ 0 & t_2\end{pmatrix},\\ M_{n,1} &= \begin{pmatrix} t_2 & 0\\ -i\frac{\gamma_n}{2} - E & t_1 + \frac{\gamma_n}{2}\end{pmatrix}.\end{aligned} \tag{9}$$

Here, $\mathcal{T}$ refers to a transpose operation, and the nth cell consists of the nth sites of chains A and B. Then, Eq. (8) directly leads to

$$|\psi(n)\rangle = T(n)|\psi(n-1)\rangle, \tag{10}$$

where $T(n)$ is a 2×2 transfer matrix between the $(n-1)$th and nth unit cells, given by

$$T(n) = -M_{n,1}^{-1}M_{n,0} = \begin{pmatrix} T_{00} & T_{01}\\ T_{10} & T_{11}\end{pmatrix}, \tag{11}$$

where the matrix elements are

$$\begin{aligned} T_{00} &= -\frac{t_1 - \gamma_{n-1}/2}{t_2},\\ T_{01} &= \frac{E + i\gamma_{n-1}/2}{t_2},\\ T_{10} &= -\frac{(E + i\gamma_n/2)(t_1 - \gamma_{n-1}/2)}{t_2(t_1 + \gamma_n/2)},\\ T_{11} &= \frac{(E + i\gamma_{n-1}/2)(E + i\gamma_n/2) - t_2^2}{t_2(t_1 + \gamma_n/2)}.\end{aligned} \tag{12}$$

If γ_n is uniform, then $T(n)$ simplifies to a constant matrix T_0. As a result, we have $|\psi(n)\rangle = (T_0)^{n-1}|\psi(1)\rangle$, which reduces to the ansatz of non-Bloch band theory.

B. Convergence of transfer-matrix eigenvalues

In our model, $T(n)$ is a function of n, and its eigenequation can be written as

$$\lambda^2(n) + b(n)\lambda(n) + c(n) = 0. \tag{13}$$

Here,

$$\begin{aligned} b(n) &= \frac{t_1^2 + t_2^2 - E^2 + \gamma_n^- t_1 - i\gamma_n^+ E}{t_2(t_1 + \gamma_n/2)},\\ c(n) &= \frac{t_1 - \gamma_{n-1}/2}{t_1 + \gamma_n/2},\end{aligned} \tag{14}$$

with $\gamma_n^\pm = (\gamma_n \pm \gamma_{n-1})/2$. It is clear that the two eigenvalues of the transfer matrix $T(n)$ are $\lambda^\pm(n) = [-b(n) \pm \sqrt{b^2(n) - 4c(n)}]/2$, corresponding to the left and right eigenvectors $\langle\lambda_L^\pm(n)|$ and $|\lambda_R^\pm(n)\rangle$, which are orthonormal and complete. Here, we note that the transfer matrix in our model is inherently non-Hermitian and may, in principle, exhibit exceptional points at specific combinations of site index n and energy E, where the two eigenvalues of the matrix coalesce [93,94]. While a systematic analysis of such degeneracies is beyond the scope of this work, we consider this an interesting direction for future exploration.

Since $b(n)$ and $c(n)$ converge to $-2iE/t_2$ and -1, respectively, as n approaches infinity, we therefore have

$$\lim_{n\to\infty}\lambda^\pm(n) \to \lambda_0^\pm = \frac{iE}{t_2}[1 \pm \sqrt{1 - (t_2/E)^2}], \tag{15}$$

which is the same as $\beta_\pm$ in Eq. (6) obtained from the rough approach mentioned above. Recall that the "−" part of the T-shaped spectrum is $E^{0,-} = t_2\sin(k)$ in the decoupled case of chains A and B. Thus, we define $\kappa = \arcsin(E/t_2)$, which is a complex number; then, Eq. (15) becomes $\lambda_0^\pm = \pm e^{\pm i\kappa}$ [95], which corresponds to the Bloch phase factor $\pm e^{\pm ik}$ in the decoupled case. It is easily seen that $|\lambda_0^+| > 1$ and $|\lambda_0^-| < 1$ (see Appendix C for details), consistent with the numerical results [see Fig. 4(c)].

Next, we examine the convergence of $\lambda^\pm(n)$ toward $\lambda_0^\pm$. As illustrated in Fig. 4(c), $\lambda^-(n)$ converges notably faster than $\lambda^+(n)$. Here, we provide a concise idea for the proof of this result. For convenience, we assume that γ_n takes the form $\gamma_n = n\gamma_0$. The detailed proofs for various types of γ_n functions are given in Appendix E. To analyze the speed of convergence,

we perform a Laurent expansion for $\lambda^{\pm}(n)$, given by

$$\lambda^{\pm}(n) = \lambda_0^{\pm} + \lambda_1^{\pm}/\gamma_n + \cdots, \tag{16}$$

and combining Eqs. (13), (14), and (16), we obtain

$$\frac{\lambda_1^{\pm}}{\lambda_0^{\pm}} = \mp \frac{(t_1 \pm t_2\cos(\kappa))(t_1 \pm t_2\cos(\kappa) + \gamma_0/2)}{t_2\cos(\kappa)}. \tag{17}$$

Equation (17) characterizes the convergence speed of $\lambda^{\pm}(n)$; that is, a smaller value of $\lambda_1^{\pm}/\lambda_0^{\pm}$ implies a smaller $1/\gamma_n$ term, and thus a faster convergence. In the thermodynamic limit, the "−" part of the spectrum in the coupled case of chains A and B closely approximates that in the decoupled case (see Appendix D for details). Consequently, κ can be closely approximated by k in the decoupled case, which ranges from $-\pi/2$ to $\pi/2$. Then, it follows from Eq. (17) that $|\lambda_1^-/\lambda_0^-| < |\lambda_1^+/\lambda_0^+|$. In particular, $|\lambda_1^-/\lambda_0^-|$ approaches zero when $\cos(\kappa)$ is close to t_1/t_2 or $(t_1+\gamma_0/2)/t_2$, leading to a much faster convergence speed of $\lambda^-(n)$.

C. Formation of the imaginary-Stark skin effect

We can now analyze the formation of the ISSE states in our model. We decompose $|\psi(n)\rangle$ into the eigenvectors of $T(n)$:

$$|\psi(n)\rangle = \psi_n^+|\lambda_R^+(n)\rangle + \psi_n^-|\lambda_R^-(n)\rangle, \tag{18}$$

where $\psi_n^{\pm} = \langle\lambda_L^{\pm}(n)|\psi(n)\rangle$. If γ_n is uniform, then $\lambda^{\pm}(n) = \lambda^{\pm}$ is constant. Together with Eq. (10), we obtain $\psi_n^{\pm} = \lambda^{\pm}\psi_{n-1}^{\pm}$, which aligns with the intuition that $\psi_n^{\pm}$ are scaled by the corresponding eigenvalues $\lambda^{\pm}$. When returning to the nonuniform γ_n and assuming that the transfer matrix $T(n)$ varies slowly, we can take the approximation (see Appendix F for details)

$$\psi_n^{\pm} \approx \lambda^{\pm}(n)\psi_{n-1}^{\pm}. \tag{19}$$

Figure 4(d) shows how $\psi_n^{\pm}$ evolves with n. The components of $|\psi(n)\rangle$, namely, ψ_n^+ and ψ_n^-, need to be of the same order at the two edges, so that they can cancel each other to satisfy the OBCs $|\psi(0)\rangle = |\psi(L+1)\rangle = 0$. We divide the wave function $\psi_n^{\pm}$ into three regions, labeled by I, II, and III, as in Figs. 4(c) and 4(d). These three regions can be roughly viewed as the left-boundary, bulk, and right-boundary regions, respectively. In region I, near the left edge, ψ_n^+ and ψ_n^- have the same order. The eigenvalue $\lambda^-(n)$ converges to λ_0^- quickly, so according to Eq. (F3), $\psi_n^- \sim (\lambda_0^-)^n$ behaves like an exponentially decaying wave. Moreover, as γ_n increases from 0 to $2t_1$, $\lambda^+(n) = c(n)/\lambda^-(n) \approx c(n)/\lambda_0^-$ approaches 0. Hence, $|\psi_n^+|$ decays much faster than $|\psi_n^-|$, ultimately reaching an extremely low value. In region II, $|\psi_n^+|$ is several orders of magnitude lower than $|\psi_n^-|$, so ψ_n^- dominates the behavior of the state $|\psi(n)\rangle$ and has a rigorously exponential decay. As n grows, $|\lambda^+(n)|$ monotonically increases to $|\lambda_0^+|$. When $|\lambda^+(n)| > 1$, it signifies a transition to region III, near the right boundary. In this region, $|\psi_n^+|$ starts to increase, and ultimately approaches the order of $|\psi_n^-|$ at the right edge, to satisfy the OBCs. Examining these regions reveals that $|\psi_n^-|$ is much larger than $|\psi_n^+|$ in the bulk. Therefore, the $\psi_n^-|\lambda_R^-(n)\rangle$ term of Eq. (18) dominates the behavior of $|\psi(n)\rangle$, which scales as $(\lambda_0^-)^n$. In contrast, the $\psi_n^+|\lambda_R^+(n)\rangle$ term becomes dominant only near the boundaries, thus causing fluctuations in the wave function at these areas [see Fig. 4(b)].

Our analysis shows that the formation of the ISSE in our model demands a notably fast convergence speed of $\lambda^-(n)$, leading to a single stable exponentially decaying wave that predominantly governs the behavior of the skin modes in the bulk. We also discuss the impact of parameters in Appendix F. An extremely small or large t_1, compared to t_2, can result in a slow convergence speed of $\lambda^-(n)$, which weakens the features of the ISSE. This also supports the relationship between the ISSE and the convergence speed of $\lambda^-(n)$. Furthermore, we demonstrate that it is possible to show the ISSE in a short lattice, which provides the feasibility of future experimental investigations with finite-size systems.

V. CONCLUSIONS

We unveil a class of NHSE, the ISSE, arising in a nonuniform lossy lattice. Unlike the conventional NHSE described by non-Bloch band theory, the ISSE exhibits a single dominant exponentially decaying wave within the bulk. Such a peculiar behavior is closely related to the convergence speed of the transfer-matrix eigenvalues. The eigendecomposition of the transfer matrix reveals that the wave function comprises two parts: a dominant, exponentially decaying component that governs bulk behavior and a negligible component that is impactful only at the boundaries. Our work provides a new perspective for accurately quantifying the NHSE in translational symmetry-breaking systems and can be extended to other models, e.g., Floquet systems with nonuniform dissipation [96,97], interacting non-Hermitian system [98–100], and Liouvillian skin effect [101–103].

ACKNOWLEDGMENTS

The authors would like to thank Professor Jieqiao Liao, Dr. Pengyu Wen, and Dr. Chenyang Wang for helpful discussion. This work was supported by the National Natural Science Foundation of China under Grants No. 11974205 and No. 61727801, and the Key Research and Development Program of Guangdong Province (2018B030325002). W.Q. acknowledges support of the National Natural Science Foundation of China (NSFC) via Grant No. 0401260012. F.N. was supported in part by the Japan Science and Technology Agency (JST) [via the CREST Quantum Frontiers program Grant No. JPMJCR24I2, the Quantum Leap Flagship Program (Q-LEAP), and the Moonshot R&D Grant No. JPMJMS2061].

DATA AVAILABILITY

No data were created or analyzed in this study.

APPENDIX A: DYNAMICAL BEHAVIOR OF INITIALLY LOCALIZED STATES

In this section, we analyze the distinct dynamical behavior of an initially localized state, depending on whether it is prepared on chain A or chain B, reflecting the intrinsic differences between the eigenstates associated with each sublattice.

For simplicity, we treat the initial state as a particle, which is placed on site (x_0, A) or (x_0, B) at time $t = 0$. When

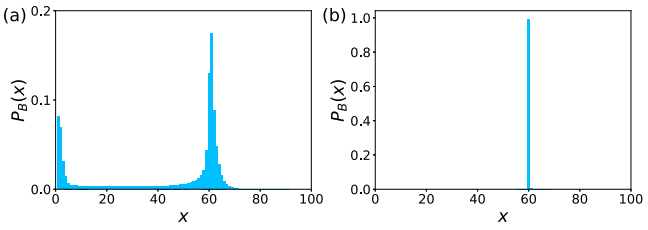

FIG. 5. The escape probability $P_B(x)$ for a particle initialized on (a) site (x_0, A) and (b) site (x_0, B). The parameters are $L = 100$, $x_0 = 60$, $t_1 = 0.4$, $t_2 = 0.5$, and loss rate $\gamma_n = 0.1n$.

the particle is initially placed on chain A, previous works [30,84,104] have shown that a peculiar non-Hermitian dynamical phenomenon—known as the edge burst—can emerge. Specifically, the particle spreads in both directions along chain A and gradually escapes from chain B due to the on-site dissipation. One might intuitively expect the escape probability on site (x, B), denoted as $P_B(x)$, to exhibit a single, asymmetric peak centered around the initial position x_0. However, under certain conditions, a distinct peak can emerge at the left boundary, as demonstrated in Fig. 5(a). This edge burst occurs when two criteria are met:

(1) The system exhibits an NHSE, which favors motion toward the boundary.

(2) The system supports eigenstates with purely real energy eigenvalues, enabling long-range propagation without exponential decay.

Under these conditions, the particle can propagate toward the boundary in a power-law decay fashion, retaining significant probability amplitude that subsequently leaks into chain B near the edge. This mechanism has been first theoretically studied in Ref. [30] for uniform loss rate. Then, Refs. [84,104] explored the generalization of the edge burst in systems with nonuniform and spatially varying loss rate.

In contrast, if the particle is initially prepared on chain B, the dynamical behavior is considerably simpler. Due to the local imaginary potential, the particle experiences strong on-site dissipation and decays rapidly without significant spatial spreading. This is illustrated in Fig. 5(b), where the escape probability $P_B(x)$ remains localized near the initial position with minimal broadening [105]. This stark contrast in dynamics further reflects the distinction we highlighted in the main text: While chain A hosts skin modes, the eigenstates in chain B are localized within bulk, resembling Wannier-Stark localization.

APPENDIX B: ROTATION TRANSFORMATION ON THE HAMILTONIAN

The Hamiltonian of our model is given by

$$\hat{H} = i\frac{t_2}{2}\sum_{n=1}^{L-1}[|n+1,A\rangle\langle n,A| - |n+1,B\rangle\langle n,B|] + \frac{t_2}{2}\sum_{n=1}^{L-1}[|n+1,B\rangle\langle n,A| + |n+1,A\rangle\langle n,B|] + t_1\sum_{n=1}^{L}|n,A\rangle\langle n,B| + \text{H.c.} - \sum_{n=1}^{L} i\gamma_n|n,B\rangle\langle n,B|. \tag{B1}$$

We regard each unit cell as a pseudospin. Specifically, we define $|n,A\rangle$ as $|\sigma_z^n = +\frac{1}{2}\rangle$ and $|n,B\rangle$ as $|\sigma_z^n = -\frac{1}{2}\rangle$. Then, we apply a $\pi/2$ rotation transformation along the x axis to each spin, i.e.,

$$\hat{H}' = \mathcal{R}^{-1}\hat{H}\mathcal{R}, \tag{B2}$$

where $\mathcal{R}$ is the spin rotation operator given by

$$\mathcal{R} = \bigoplus_n \exp\left(-i\frac{\pi}{4}\sigma_x^n\right). \tag{B3}$$

After the rotation, the Hamiltonian becomes

$$\hat{H}' = t_2\sum_{n=1}^{L-1}|n+1,A'\rangle\langle n,B'| + \text{H.c.} + \sum_{n=1}^{L}\left[\left(t_1+\frac{\gamma_n}{2}\right)|n,A'\rangle\langle n,B'| + \left(t_1-\frac{\gamma_n}{2}\right)|n,B'\rangle\langle n,A'|\right] - i\frac{\gamma_n}{2}\sum_{n=1}^{L}[|n,A'\rangle\langle n,A'| + |n,B'\rangle\langle n,B'|], \tag{B4}$$

where $|n,A'\rangle$ and $|n,B'\rangle$ are the new Z bases of the pseudospin after the rotation. The transformation of the wave function is given by

$$\begin{pmatrix}\psi_n^{A'}\\ \psi_n^{B'}\end{pmatrix} = \mathcal{R}^{-1}\begin{pmatrix}\psi_n^{A}\\ \psi_n^{B}\end{pmatrix}, \tag{B5}$$

that is,

$$\psi_n^{A'} = \frac{\sqrt{2}}{2}\psi_n^A + i\frac{\sqrt{2}}{2}\psi_n^B,$$
$$\psi_n^{B'} = i\frac{\sqrt{2}}{2}\psi_n^A + \frac{\sqrt{2}}{2}\psi_n^B. \tag{B6}$$

APPENDIX C: THE MODULUS OF THE PARAMETERS $\lambda_0^{\pm}$

Let us begin with the following conclusion from the main text:

$$\lambda_0^{\pm} = \pm\exp(\pm i\kappa), \tag{C1}$$

where $\kappa = \arcsin(E/t_2)$ is a complex number. Given that our system is dissipative, the imaginary part of the eigenenergy is negative, i.e., $\text{Im}(E) < 0$. Therefore, the imaginary part of κ,

namely, $\mathrm{Im}(\kappa)$, is also negative, indicating that

$$|\lambda_0^+| = \exp[-\mathrm{Im}(\kappa)] > 1,$$
$$|\lambda_0^-| = \exp[\mathrm{Im}(\kappa)] < 1. \tag{C2}$$

APPENDIX D: ENERGY DIFFERENCE BETWEEN THE DECOUPLED AND COUPLED CONFIGURATIONS OF CHAINS A AND B

In this section, we show that the energy difference in the "−" horizontal part of the T-shaped spectrum, between the decoupled and coupled configurations of chains A and B, vanishes in the thermodynamic limit. For clarity, we introduce the following notations for these two system configurations. The Hamiltonian in the decoupled case is denoted as H^0, while the Hamiltonian in the coupled case is represented as H. The difference between these Hamiltonians, denoted by ΔH, is defined as $\Delta H := H - H^0$. The right eigenstates of H^0 are denoted by $|R_i^0\rangle$ with corresponding eigenenergies E_i^0, where the subscript i is the index of the eigenstates. Furthermore, we specify $E_i^{0,-}$ ($E_i^{0,|}$) and $|R_i^{0,-}\rangle$ ($|R_i^{0,|}\rangle$) as the eigenenergies and eigenstates belonging to the "−" ("|") subspace of the H^0 spectrum, respectively. We use similar notations E_i, E_i^-, and $E_i^|$ to denote the corresponding energy spectra in the coupled case.

In the decoupled case of chains A and B, for the "−" part of the spectrum, the eigenenergies are given by $E_i^{0,-} = t_2 \sin k$, where $k = (\frac{i}{L+1} - \frac{1}{2})\pi$ and $i = 1, 2, \ldots, L$. The corresponding eigenstates are the extended standing waves in the bulk, expressed as

$$|R_i^{0,-}\rangle = \sqrt{\frac{2}{L}} \sum_{n=1}^{L} (-1)^{n/2} \sin\left[\left(\frac{\pi}{2} - k\right)n\right] |n, A\rangle. \tag{D1}$$

For the "|" vertical part of the spectrum, the eigenstates are localized around the sites of chain B, with energies that are approximately equal to $-i\gamma_n$.

Now, we focus on the energy difference in the "−" part, between the decoupled and coupled cases of chains A and B, based on the following assumption:

Assumption 1. Define $H(t) := H^0 + t\Delta H$ for $t \in [0, 1]$, such that $H(0) = H^0$ and $H(1) = H$. Consider an eigenvalue in the "−" part of the spectrum of H^0, denoted as $E_i^{0,-}$, along with its corresponding eigenvalue E_i^- in the "−" part of the spectrum of H. As the parameter t varies, the eigenvalue of $H(t)$ traces a trajectory, denoted by $E_i(t)$. This trajectory connects E_i^0 to E_i, meaning that $E_i(0) = E_i^{0,-}$ and $E_i(1) = E_i^-$, without any level crossings.

This assumption is akin to the adiabatic assumption in Hermitian systems. Based on this assumption, we argue that the energy from the "−" part in the decoupled case of chains A and B converges to that in the coupled cases; namely, $E_i^{0,-} \sim E_i^-$ in the thermodynamic limit.

In Fig. 6, we show that the average energy difference,

$$\Delta E = \overline{|E_i^{0,-} - E_i^-|}, \tag{D2}$$

decreases as the chain length L increases. This reduction in ΔE can be attributed to two primary factors. First, as L increases, the average separation between energies from the "−" part and the "|" part also increases, scaling as γ_n.

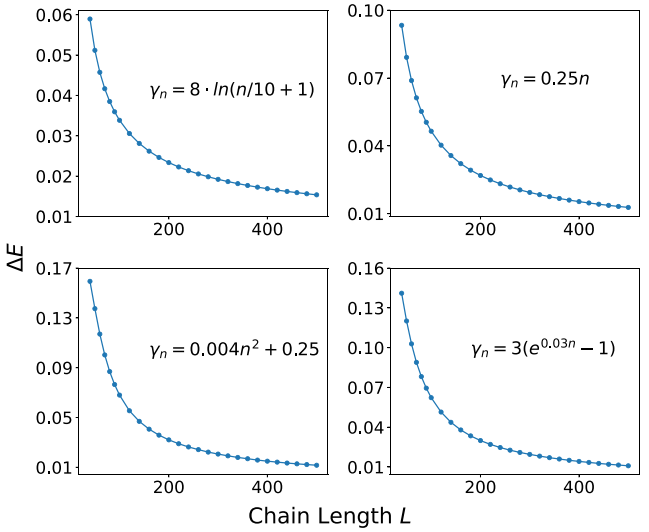

FIG. 6. Average energy difference in the "−" part of the spectrum between the decoupled and coupled cases, given by $\Delta E = (N^{0,-})^{-1} \sum_i |E_i^{0,-} - E_i^-|$, where $N^{0,-} = |\{E_i^{0,-}\}_i|$ denotes the number of eigenenergies in the "−" part of the spectrum. This difference is depicted as a function of chain length L for logarithmic, linear, quadratic, and exponential loss rate functions. The parameters are $t_1 = 0.4$ and $t_2 = 0.5$.

Second, consider the strength of the couplings, introduced by the perturbation ΔH, between the state $|R_i^{0,-}\rangle$ and the eigenstates from the "|" part. Here, the eigenstates from the "|" part are localized states around the sites of chain B, denoted by (n, B), and ΔH is a local coupling. Due to this localized nature, through ΔH, the eigenstates from the "|" part can only couple with the portion of the wave function that is near (n, B). However, the state $|R_i^{0,-}\rangle$ is an extended standing wave, with an amplitude that diminishes with L, scaling as $\sqrt{1/L}$. Therefore, the coupling between the state $|R_i^{0,-}\rangle$ and the eigenstates from the "|" part weakens as L increases. These two factors collectively contribute to the attenuation of the virtual process between the eigenstates from the "−" part and the "|" part, resulting in a diminishing energy perturbation.

To elaborate further, we can use eigenvalue perturbation theory to analyze this model, by treating ΔH as the perturbation acting on H^0 [106]. Since ΔH only couples adjacent A and B sites, the first-order perturbation of $E_i^{0,-}$ is zero. Instead, the dominant perturbation term arises from the second-order process between the eigenstate of $E_i^{0,-}$ and the eigenstates of the "|" part spectrum, represented by

$$E_i^{2,-} = \sum_j \frac{\langle L_i^{0,-}|\Delta H|R_j^{0,|}\rangle\langle L_j^{0,|}|\Delta H|R_i^{0,-}\rangle}{E_i^{0,-} - E_j^{0,|}}, \tag{D3}$$

where $\langle L_i^{0,-}|$ and $\langle L_j^{0,|}|$ are the left eigenstates corresponding to $E_i^{0,-}$ and $E_j^{0,|}$, respectively. In the term $\langle L_i^{0,-}|\Delta H|R_j^{0,|}\rangle$ of Eq. (D3), the state $|R_j^{0,|}\rangle$ is a localized wave function with a width of $w(j) \sim w_0/\gamma_j'$, where w_0 is a constant and $\gamma_j' = \frac{d\gamma_n}{dn}|_{n=j}$. This phenomenon is similar to the Wannier-Stark localization [88,89]. Since ΔH only couples adjacent A and B sites, $\Delta H|R_j^{0,|}\rangle$ also yields a localized wave function with a

width approximately equal to $w(j)$. Thus, its norm satisfies

$$\left|\Delta H\left|R_j^{0,|}\right\rangle\right| \leqslant (t_1+t_2)\left|\left|R_j^{0,|}\right\rangle\right| = t_1+t_2, \tag{D4}$$

where (t_1+t_2) is the largest eigenvalue of ΔH. In contrast, the state $\langle L_i^{0,-}| = \sqrt{\frac{2}{L}}\sum_{n=1}^{L}(-1)^{n/2}\sin[(\frac{\pi}{2}-k)n]\langle n,A|$ represents a standing wave, which is extended in the bulk. As a result, the matrix element $\langle L_i^{0,-}|\Delta H|R_j^{0,|}\rangle$ is bounded by

$$\begin{aligned}\left|\left\langle L_i^{0,-}\right|\Delta H\left|R_j^{0,|}\right\rangle\right| &\leqslant (t_1+t_2)\sqrt{\frac{2}{L}}w(j)\\ &= \mathcal{O}\left(\frac{1}{\gamma_j'\sqrt{L}}\right),\end{aligned} \tag{D5}$$

where $\mathcal{O}$ denotes the big O notation, which describes the limiting behavior of a function. For the denominator $(E_i^{0,-}-E_j^{0,|})$ in Eq. (D3), since $|E_j^{0,|}| \gg |E_i^{0,-}|$, we can derive the inequality

$$\begin{aligned}\left|E_i^{0,-}-E_j^{0,|}\right| &\geqslant \left|E_j^{0,|}\right| - \left|E_i^{0,-}\right|\\ &\geqslant \gamma_j - t_2 - t_2 = \gamma_j - 2t_2.\end{aligned} \tag{D6}$$

By combining inequalities (D5) and (D6), the upper bound of $E_i^{2,-}$ can be expressed as

$$\begin{aligned}E_i^{2,-} &\leqslant \frac{C}{L}\sum_j \frac{1}{\gamma_j'^2(\gamma_j-2t_2)}\\ &= \mathcal{O}\left(\frac{1}{L}\sum_j \frac{1}{\gamma_j'^2\gamma_j}\right),\end{aligned} \tag{D7}$$

where C is a relevant constant. For a polynomial loss rate $\gamma_n = n^\alpha$, with $\alpha \geqslant 1$, or an exponential loss rate, it follows that

$$\lim_{L\to\infty}\frac{1}{L}\sum_j \frac{1}{\gamma_j'^2\gamma_j} = 0, \tag{D8}$$

which implies that the second-order perturbation of the energy $E_i^{2,-}$ converges to zero in the thermodynamic limit. Although this upper bound diverges for a logarithmic loss rate, numerical results suggest that, for a logarithmic loss rate function, the average energy difference in the "−" part between the decoupled and coupled configurations of chains A and B also decreases as the chain length L increases (see Fig. 6).

Upon $E_i^- \sim E_i^{0,-}$, one might raise the question of why an NHSE state and an extended state share similar energy values. In fact, as the parameter L increases, the NHSE weakens, and the decay rate λ_0^- of the wave function tends toward 1, as illustrated in Fig. 7. This makes the wave function more akin to an extended state. This phenomenon aligns with the physical intuition that a larger lattice implies a greater average loss rate in this model. Additionally, a lattice with a uniform loss rate will exhibit a weaker NHSE when the loss rate is larger.

APPENDIX E: CONVERGENCE OF THE TRANSFER-MATRIX EIGENVALUES $\lambda^{\pm}(n)$

In the main article, we state that $\lambda^-(n)$ converges much faster than $\lambda^+(n)$. In this section, we delve into the convergence properties of $\lambda^{\pm}(n)$ in detail and establish the validity of this assertion across a broad range of types of the function γ_n.

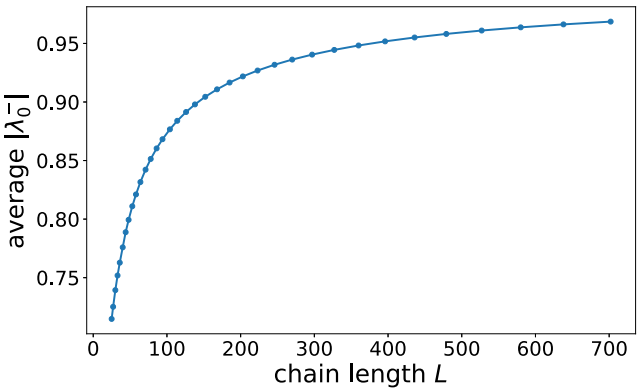

FIG. 7. Average of $|\lambda_0^-|$ over eigenstates in the "−" part of the spectrum as a function of chain length L. The average $|\lambda_0^-|$ increases monotonically and tends to approach 1 as L increases. The parameters are $t_1 = 0.4$, $t_2 = 0.5$, and $\gamma_n = 0.25n$.

According to Eq. (14), $b(n)$ and $c(n)$ converge to the constant values b_0 and c_0, respectively, as n approaches infinity. For example, we have

$$\begin{aligned}\lim_{n\to\infty} b(n) &\to b_0 = -2iE/t_2,\\ \lim_{n\to\infty} c(n) &\to c_0 = -1,\end{aligned} \tag{E1}$$

for the polynomial loss rate $\gamma_n = n^\alpha$. Consequently, $\lambda^{\pm}(n)$ converge to

$$\begin{aligned}\lim_{n\to\infty}\lambda^{\pm}(n) \to \lambda_0^{\pm} &= \frac{1}{2}\left(-b_0 \pm \sqrt{b_0^2-4c_0}\right)\\ &= \frac{iE}{t_2}[1\pm\sqrt{1-(t_2/E)^2}].\end{aligned} \tag{E2}$$

To analyze the convergence properties of $\lambda^{\pm}(n)$, we expand Eq. (14) in terms of $1/\gamma_n$, yielding

$$\begin{aligned}b(n) &= b_0 + \frac{\gamma_n-\gamma_{n-1}}{\gamma_n}\frac{t_1+iE}{t_2}\\ &\quad + \frac{1}{\gamma_n}\frac{2\left(t_1^2+t_2^2-E^2+2iEt_1\right)}{t_2} + \frac{b_2}{\gamma_n^2}+\cdots,\\ c(n) &= c_0 + \frac{\gamma_n-\gamma_{n-1}}{\gamma_n} + \frac{4t_1}{\gamma_n} + \frac{c_2}{\gamma_n^2}+\cdots,\end{aligned} \tag{E3}$$

where b_2 and c_2 are the coefficients of the $(1/\gamma_n)^2$ terms. To isolate the leading-order contribution, we neglect higher-order terms $(1/\gamma_n)^m$ for $m>1$, retaining only the $1/\gamma_n$ and $(\gamma_n-\gamma_{n-1})/\gamma_n$ terms. The specific form of γ_n determines which one is the leading nontrivial term. We will discuss several different types of the function γ_n in the following.

(1) $\lim_{n\to\infty}(\gamma_n-\gamma_{n-1}) = 0$. For example, consider a logarithmic function $\gamma_n \sim \log n$, or a polynomial function of degree smaller than 1, i.e., $\gamma_n \sim n^\alpha$, where $0<\alpha<1$.

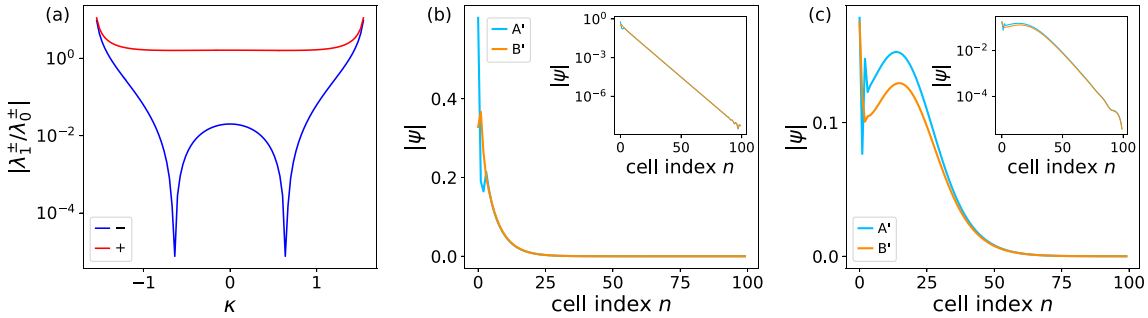

FIG. 8. (a) $|\lambda_1^{\pm}/\lambda_0^{\pm}|$ as a function of κ, under the condition that $\lim_{n\to\infty}(\gamma_n - \gamma_{n-1}) = 0$. Here, κ ranges from $-\pi/2$ to $\pi/2$. (b), (c) Profiles of eigenstates, with insets showing the eigenstates on a logarithmic scale. $\gamma_n = 20\ln(1 + n/100)$. For panel (b), the energy is $E = -0.270 - 0.079i$ ($\kappa = -0.560 - 0.185i$). For (c), $E = -0.485 - 0.025i$ ($\kappa = -1.272 - 0.168i$). Throughout panels (a)–(c), $t_1 = 0.4$ and $t_2 = 0.5$.

In this type of γ_n function, it is apparent that the leading nontrivial term is the $1/\gamma_n$ term. By taking the first-order approximation of Eq. (E3), we obtain

$$\begin{aligned} b(n) &= b_0 + \frac{b_1}{\gamma_n} + \cdots, \\ c(n) &= c_0 + \frac{c_1}{\gamma_n} + \cdots, \\ \text{where} \quad b_1 &= \frac{2\left(t_1^2 + t_2^2 - E^2 + 2iEt_1\right)}{t_2}, \\ c_1 &= 4t_1. \end{aligned} \tag{E4}$$

Similarly, the expansion of $\lambda^{\pm}(n)$ is

$$\lambda^{\pm}(n) = \lambda_0^{\pm} + \frac{\lambda_1^{\pm}}{\gamma_n} + \cdots, \tag{E5}$$

where $\lambda_1^{\pm}$ represents the expansion coefficient of the $1/\gamma_n$ term. By substituting Eqs. (E4) and (E5) into Eq. (13), we can derive the ratio $\lambda_1^{\pm}/\lambda_0^{\pm}$:

$$\frac{\lambda_1^{\pm}}{\lambda_0^{\pm}} = -\frac{b_1 + c_1/\lambda_0^{\pm}}{2\lambda_0^{\pm} + b_0}. \tag{E6}$$

The quantity $\lambda_1^{\pm}/\lambda_0^{\pm}$ characterizes the convergence speed of $\lambda^{\pm}(n)$; specifically, a smaller value of $\lambda_1^{\pm}/\lambda_0^{\pm}$ indicates a smaller $1/\gamma_n$ term, resulting in a faster convergence to $\lambda_0^{\pm}$.

In the decoupled case of chains A and B, the "$-$" part of the T-shaped spectrum is characterized by $E^{0,-} = t_2 \sin k$, where $k = (\frac{i}{L+1} - \frac{1}{2})\pi$, and $i = 1, 2, \ldots, L$. Analogously, we define $\kappa = \arcsin(E/t_2)$. Consequently, Eq. (E2) becomes

$$\lambda_0^{\pm} = \pm\exp(\pm i\kappa), \tag{E7}$$

which corresponds to the Bloch phase factor $\pm e^{\pm ik}$. By substituting Eqs. (E4) and (E7) into Eq. (E6), we have

$$\frac{\lambda_1^{\pm}}{\lambda_0^{\pm}} = \mp\frac{(t_1 \pm t_2\cos(\kappa))^2}{t_2\cos(\kappa)}. \tag{E8}$$

In Appendix D, we argue that in the thermodynamic limit, the "$-$" part of the spectrum in the coupled case of chains A and B converges toward that of the decoupled case. As a result, the parameter κ in Eq. (E8) can be closely approximated by k in the decoupled case, which spans the range from $-\pi/2$ to $\pi/2$. Then, it follows from Eq. (E8) that $|\lambda_1^-/\lambda_0^-|$ is always smaller than $|\lambda_1^+/\lambda_0^+|$, as shown in Fig. 8(a). Especially, the ratio $|\lambda_1^-/\lambda_0^-|$ approaches zero when $\cos(\kappa)$ is close to t_1/t_2, which significantly accelerates the convergence of $\lambda^-(n)$ and exhibits typical ISSE [Fig. 8(b)]. As κ approaches $\pm\pi/2$, the ratio $|\lambda_1^{\pm}/\lambda_0^{\pm}|$ diverges to infinity, which causes the ISSE to become less apparent [Fig. 8(c)].

(2) $\lim_{n\to\infty}(\gamma_n - \gamma_{n-1}) = \gamma_0$, where γ_0 is a constant. For example, consider linear function $\gamma_n = \gamma_0 n$.

In this type of γ_n function, both the $1/\gamma_n$ and $(\gamma_n - \gamma_{n-1})/\gamma_n$ terms exhibit leading nontrivial contributions. Thus, the leading terms of $b(n)$, $c(n)$, and $\lambda^{\pm}(n)$ are given by

$$\begin{aligned} b(n) &= b_0 + \frac{b_1}{\gamma_n} + \cdots, \\ c(n) &= c_0 + \frac{c_1}{\gamma_n} + \cdots, \\ \text{where} \quad b_1 &= \frac{(t_1 + iE)\gamma_0 + 2\left(t_1^2 + t_2^2 - E^2 + 2iEt_1\right)}{t_2}, \\ c_1 &= 4t_1 + \gamma_0, \\ \lambda^{\pm}(n) &= \lambda_0^{\pm} + \frac{\lambda_1^{\pm}}{\gamma_n} + \cdots. \end{aligned} \tag{E9}$$

Since the forms of $b(n)$, $c(n)$, and $\lambda^{\pm}(n)$ are identical to those in type (1), $\lambda_1^{\pm}/\lambda_0^{\pm}$ can be derived using the same method. This yields

$$\frac{\lambda_1^{\pm}}{\lambda_0^{\pm}} = \mp\frac{(t_1 \pm t_2\cos(\kappa))(t_1 \pm t_2\cos(\kappa) + \gamma_0/2)}{t_2\cos(\kappa)}. \tag{E10}$$

The magnitude of the ratio $|\lambda_1^-/\lambda_0^-|$ is generally smaller than that of $|\lambda_1^+/\lambda_0^+|$. Notably, as $\cos(\kappa)$ approaches either t_1/t_2 or $(t_1 + \gamma_0/2)/t_2$, the value of $|\lambda_1^-/\lambda_0^-|$ tends to zero.

(3) $\lim_{n\to\infty}(\gamma_n - \gamma_{n-1}) = \infty$, but $\lim_{n\to\infty}\frac{\gamma_n - \gamma_{n-1}}{\gamma_n} = 0$. For example, consider a polynomial function with a degree greater than 1, $\gamma_n \sim n^{\alpha}$, where $\alpha > 1$.

In this case, the leading nontrivial term is $(\gamma_n - \gamma_{n-1})/\gamma_n$. Upon expanding $b(n)$, $c(n)$, and $\lambda^{\pm}(n)$ to the first-order

approximation, we obtain

$$b(n) = b_0 + b_1\frac{\gamma_n - \gamma_{n-1}}{\gamma_n} + \cdots, \quad b_1 = \frac{t_1 + iE}{t_2},$$
$$c(n) = c_0 + c_1\frac{\gamma_n - \gamma_{n-1}}{\gamma_n} + \cdots, \quad c_1 = 1,$$
$$\lambda^{\pm}(n) = \lambda_0^{\pm} + \lambda_1^{\pm}\frac{\gamma_n - \gamma_{n-1}}{\gamma_n} + \cdots. \tag{E11}$$

Using the same method as in type (1), we can derive $\lambda_1^{\pm}/\lambda_0^{\pm}$, resulting in

$$\frac{\lambda_1^{\pm}}{\lambda_0^{\pm}} = \mp\frac{t_1 \pm t_2\cos(\kappa)}{t_2\cos(\kappa)}. \tag{E12}$$

Similar to the findings in type (1), the magnitude of the ratio $|\lambda_1^-/\lambda_0^-|$ is always smaller than $|\lambda_1^+/\lambda_0^+|$. Additionally, this ratio converges to zero as $\cos(\kappa)$ approaches t_1/t_2.

(4) $\lim_{n\to\infty}(\gamma_n - \gamma_{n-1}) = \infty$ and $\lim_{n\to\infty}\frac{\gamma_n-\gamma_{n-1}}{\gamma_n} =$ constant. For example, consider the exponential function $\gamma_n \sim \exp(\alpha n)$.

In this case, the term $(\gamma_n - \gamma_{n-1})/\gamma_n$ degenerates to a constant in the expansion. Therefore, the leading nontrivial term is the $1/\gamma_n$ term. The coefficients $b(n)$ and $c(n)$ can be expanded as in Eq. (E4), with the same expressions of b_1 and c_1. However, the values of b_0 and c_0 will undergo a shift due to the term $(\gamma_n - \gamma_{n-1})/\gamma_n$. This shift only affects the value of $\lambda_0^{\pm}$, while preserving the convergence properties of $\lambda^{\pm}(n)$.

APPENDIX F: RECURRENCE RELATION OF $\psi_n^{\pm}$ AND ITS APPROXIMATION

In this section, we derive the recurrence relation for $\psi_n^{\pm}$ and discuss the approximations used in the main text.

We begin by decomposing $|\psi(n)\rangle$ into the eigenvectors of $T(n)$, using $\psi_n^{\pm} = \langle\lambda_L^{\pm}(n)|\psi(n)\rangle$ to denote the $\langle\lambda_L^{\pm}(n)|$ component of $|\psi(n)\rangle$. This decomposition can be expressed as

$$|\psi(n)\rangle = \psi_n^+|\lambda_R^+(n)\rangle + \psi_n^-|\lambda_R^-(n)\rangle. \tag{F1}$$

Substituting Eq. (F1) into Eq. (10) yields the recurrence relation between $\psi_{n-1}^{\pm}$ and $\psi_n^{\pm}$:

$$\psi_n^{\pm} = \lambda^{\pm}(n)[\langle\lambda_L^{\pm}(n)|\lambda_R^{\pm}(n-1)\rangle\psi_{n-1}^{\pm} + \langle\lambda_L^{\pm}(n)|\lambda_R^{\mp}(n-1)\rangle\psi_{n-1}^{\mp}]. \tag{F2}$$

If γ_n is uniform, i.e., the system has discrete translational symmetry, then the recurrence relation in Eq. (F2) simplifies to $\psi_n^{\pm} = \lambda^{\pm}\psi_{n-1}^{\pm}$. This result is straightforward, as the $\langle\lambda_L^{\pm}(n)|$ component is scaled by the corresponding eigenvalue $\lambda^{\pm}$. In more general scenarios, however, $\psi_n^{\pm} \neq \lambda^{\pm}(n)\psi_{n-1}^{\pm}$, which implies that if $|\psi(n-1)\rangle$ contains only the $|\lambda_R^+(n-1)\rangle$ component, then $|\psi(n)\rangle$ will have both the $|\lambda_R^+(n)\rangle$ and $|\lambda_R^-(n)\rangle$ components. This occurs because the transfer matrix $T(n-1)$ differs from $T(n)$, introducing a mixed term $\langle\lambda_L^{\pm}(n)|\lambda_R^{\mp}(n-1)\rangle\psi_{n-1}^{\mp}$. However, if we assume that the transfer matrix $T(n)$ varies slowly, then $\langle\lambda_L^{\pm}(n)|\lambda_R^{\pm}(n-1)\rangle \approx 1$ and $\langle\lambda_L^{\pm}(n)|\lambda_R^{\mp}(n-1)\rangle \approx 0$. Consequently, the recurrence relation in Eq. (F2) can be approximated as follows:

$$\psi_n^+ \approx \lambda^+(n)\psi_{n-1}^+ \quad \text{or} \quad \psi_n^- \approx \lambda^-(n)\psi_{n-1}^-, \tag{F3}$$

unless $|\psi_n^-| \gg |\psi_n^+|$ or $|\psi_n^+| \gg |\psi_n^-|$, respectively.

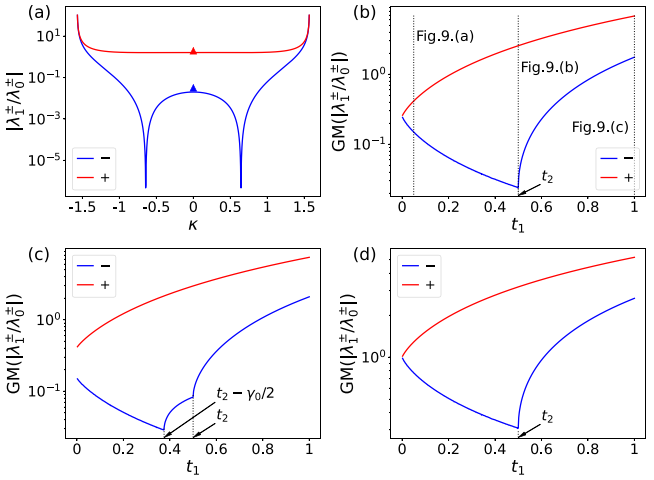

FIG. 9. (a) $|\lambda_1^{\pm}/\lambda_0^{\pm}|$ as a function of κ when t_1 and t_2 are fixed. Here, κ ranges from $-\pi/2$ to $\pi/2$. The triangle represents the geometric mean of $|\lambda_1^{\pm}/\lambda_0^{\pm}|$. The parameters are $t_1 = 0.4$, $t_2 = 0.5$, and $\gamma_n = 0.25n$. (b)–(d) Geometric mean of $|\lambda_1^{\pm}/\lambda_0^{\pm}|$ as a function of t_1, with $t_2 = 0.5$ fixed. The loss rate function γ_n satisfies $\lim_{n\to\infty}(\gamma_n - \gamma_{n-1}) = 0$ for panel (b); $\lim_{n\to\infty}(\gamma_n - \gamma_{n-1}) = \gamma_0 = 0.25$ for panel (c); and $\lim_{n\to\infty}(\gamma_n - \gamma_{n-1}) = \infty$, while $\lim_{n\to\infty}\frac{\gamma_n-\gamma_{n-1}}{\gamma_n} = 0$ for panel (d). The three vertical dotted lines in panel (b) correspond to the parameter values of Fig. 10.

APPENDIX G: ANALYSIS OF PARAMETERS

In this section, we discuss the impact of various parameters, including the hopping parameters t_1, t_2, and the chain length L, on the ISSE in our model.

1. Hopping parameters t_1 and t_2

In the main text, we state that to generate an evident ISSE, $\lambda^-(n)$ should converge to λ_0^- rapidly and at a rate significantly faster than $\lambda^+(n)$, namely,

$$|\lambda_1^-/\lambda_0^-| \ll 1, \quad |\lambda_1^-/\lambda_0^-| \ll |\lambda_1^+/\lambda_0^+|. \tag{G1}$$

Subsequently, we investigate how the hopping parameters, t_1 and t_2, impact $\lambda_1^{\pm}/\lambda_0^{\pm}$ to satisfy this condition.

In Appendix E, we show that $\lambda_1^{\pm}/\lambda_0^{\pm}$ are determined by the parameters t_1, t_2, and κ. We also argued that in the thermodynamic limit, the parameter κ can be effectively approximated by the corresponding k in the decoupled case of chains A and B, with $k \in (-\frac{\pi}{2}, \frac{\pi}{2})$. To characterize the convergence speed of $\lambda^{\pm}$ with fixed parameters t_1 and t_2, while excluding the influence of κ, we focus on the geometric mean [107] of $|\lambda_1^{\pm}/\lambda_0^{\pm}|$ across κ as a metric [Fig. 9(a)]. This choice is motivated by the fact that the arithmetic mean of $|\lambda_1^{\pm}/\lambda_0^{\pm}|$ across κ diverges in this context. The geometric mean (GM) is defined as

$$\mathrm{GM}\left(\left|\frac{\lambda_1^{\pm}}{\lambda_0^{\pm}}\right|\right) = \exp\left[\frac{1}{\pi}\int_{-\pi/2}^{\pi/2}\ln\left(\left|\frac{\lambda_1^{\pm}}{\lambda_0^{\pm}}\right|\right)d\kappa\right]. \tag{G2}$$

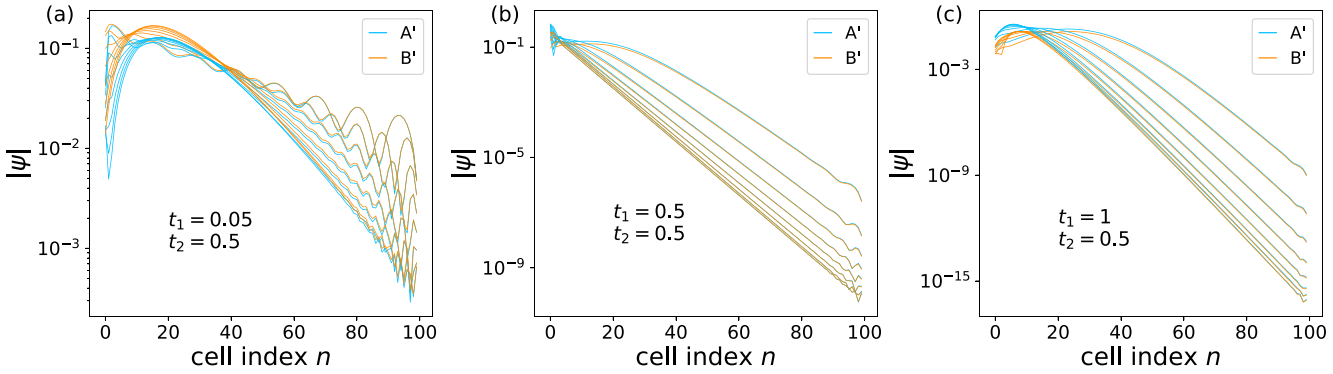

FIG. 10. Profiles of eight randomly chosen eigenstates from the "−" part of the spectrum. The parameters are $t_2 = 0.5$ and $\gamma_n = 20\ln(1 + n/100)$. For panel (a), $t_1 = 0.05$; for panel (b), $t_1 = 0.5$; and for panel (c), $t_1 = 1$. These parameter selections correspond to the illustration provided in Fig. 9(b).

We can depict $\mathrm{GM}(|\lambda_1^{\pm}/\lambda_0^{\pm}|)$ as a function of t_1 for fixed t_2 [Figs. 9(b)–9(d)].

As an illustrative example, we focus on the case where $\lim_{n\to\infty}(\gamma_n - \gamma_{n-1}) = 0$ [Fig. 9(b)]. A similar result can be shown for other types of the γ_n function. Recall the convergence speed given by Eq. (E8):

$$\frac{\lambda_1^{\pm}}{\lambda_0^{\pm}}(\kappa) = \mp\frac{(t_1 \pm t_2\cos\kappa)^2}{t_2\cos\kappa}. \tag{G3}$$

The critical point of Eq. (G3) occurs at $t_1 = t_2$, since a real zero point $\kappa = \arccos(t_1/t_2)$ exists only when $t_1 \leqslant t_2$. It is evident that $\mathrm{GM}(|\lambda_1^{+}/\lambda_0^{+}|)$ increases with t_1. In contrast, $\mathrm{GM}(|\lambda_1^{-}/\lambda_0^{-}|)$ decreases as t_1 increases from 0, reaches a minimum at the critical point $t_1 = t_2$, and then increases with t_1. Therefore, when t_1 is close to t_2, the condition stated in Eq. (G1) can be effectively satisfied, leading to typical ISSE behavior [Fig. 10(b)]. However, if t_1 is significantly smaller or larger than t_2, the features of ISSE weaken, manifesting as an initial increase followed by a decrease in the wave function from left to right, resulting in a peak near the left boundary [Figs. 10(a) and 10(c)].

2. Chain length L

In previous sections, we analyzed the model in the thermodynamic limit, where the loss rate γ_n exhibits a monotonic increase, ultimately diverging to infinity as $n \to \infty$. However, our analysis indicates that the emergence of an apparent ISSE in the model does not require the loss rate to reach this asymptotic condition. Specifically, as long as the loss rate in the lattice is sufficiently increased so that $\lambda^{-}(n)$ approaches λ_0^{-}—that is, $|(\lambda^{-}(L) - \lambda_0^{-})/\lambda_0^{-}| \ll 1$, where L is the length of the lattice—we can expect to observe an apparent ISSE. This observation suggests that the ISSE can manifest even in finite-size systems, making it feasible for future experimental investigations.

To illustrate this phenomenon, we present a numerical example featuring a linearly increasing loss rate within a short lattice configuration. In this example, the lattice length L is only 20, and the loss rate at the right boundary, γ_L, is set to 5, a value significantly below "infinity." Nevertheless, this is adequate for $\lambda^{-}(n)$ to converge to λ_0^{-} [Fig. 11(a)], which is supported by the following calculation:

$$\left|\frac{\lambda^{-}(L) - \lambda_0^{-}}{\lambda_0^{-}}\right| \approx \left|\frac{\lambda_1^{-}}{\lambda_0^{-}}\frac{1}{\gamma_L}\right| \approx 7.2 \times 10^{-3} \ll 1. \tag{G4}$$

Consequently, an apparent ISSE is observed [Fig. 11(b)], characterized by a uniform decay rate and the absence of interference.

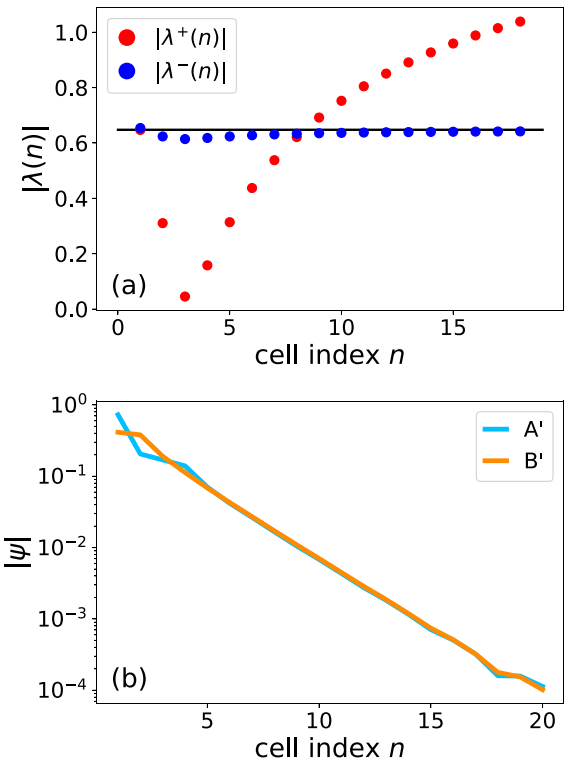

FIG. 11. (a) Modulus of $\lambda^{\pm}(n)$ and (b) profile of eigenstate $|\psi|$ as functions of cell index n, for an eigenstate where $|\lambda_1^{-}/\lambda_0^{-}| \approx 3.78 \times 10^{-2}$, in a short lattice of length $L = 20$. The energy of this eigenstate is $E \approx -0.291 - 0.190i$. The parameters are $t_1 = 0.4$, $t_2 = 0.5$, and $\gamma_n = 0.25n$. The horizontal black line in panel (a) represents λ_0^{-}.

[1] R. El-Ganainy, K. G. Makris, M. Khajavikhan, Z. H. Musslimani, S. Rotter, and D. N. Christodoulides, Non-Hermitian physics and $\mathcal{PT}$ symmetry, Nat. Phys. **14**, 11 (2018).

[2] N. Hatano and D. R. Nelson, Localization transitions in non-Hermitian quantum mechanics, Phys. Rev. Lett. **77**, 570 (1996).

[3] N. Hatano and D. R. Nelson, Vortex pinning and non-Hermitian quantum mechanics, Phys. Rev. B **56**, 8651 (1997).

[4] N. Hatano and D. R. Nelson, Non-Hermitian delocalization and eigenfunctions, Phys. Rev. B **58**, 8384 (1998).

[5] C. M. Bender and S. Boettcher, Real spectra in non-Hermitian Hamiltonians having $\mathcal{PT}$ symmetry, Phys. Rev. Lett. **80**, 5243 (1998).

[6] M. V. Berry, Physics of non-Hermitian degeneracies, Czech. J. Phys. **54**, 1039 (2004).

[7] M. S. Rudner and L. S. Levitov, Topological transition in a non-Hermitian quantum walk, Phys. Rev. Lett. **102**, 065703 (2009).

[8] A. Guo, G. J. Salamo, D. Duchesne, R. Morandotti, M. Volatier-Ravat, V. Aimez, G. A. Siviloglou, and D. N. Christodoulides, Observation of $\mathcal{PT}$-symmetry breaking in complex optical potentials, Phys. Rev. Lett. **103**, 093902 (2009).

[9] C. E. Rüter, K. G. Makris, R. El-Ganainy, D. N. Christodoulides, M. Segev, and D. Kip, Observation of parity–time symmetry in optics, Nat. Phys. **6**, 192 (2010).

[10] L. Feng, M. Ayache, J. Huang, Y.-L. Xu, M.-H. Lu, Y.-F. Chen, Y. Fainman, and A. Scherer, Nonreciprocal light propagation in a silicon photonic circuit, Science **333**, 729 (2011).

[11] A. Regensburger, C. Bersch, M.-A. Miri, G. Onishchukov, D. N. Christodoulides, and U. Peschel, Parity–time synthetic photonic lattices, Nature (London) **488**, 167 (2012).

[12] B. Zhen, C. W. Hsu, Y. Igarashi, L. Lu, I. Kaminer, A. Pick, S.-L. Chua, J. D. Joannopoulos, and M. Soljačić, Spawning rings of exceptional points out of Dirac cones, Nature (London) **525**, 354 (2015).

[13] C. Poli, M. Bellec, U. Kuhl, F. Mortessagne, and H. Schomerus, Selective enhancement of topologically induced interface states in a dielectric resonator chain, Nat. Commun. **6**, 6710 (2015).

[14] S. Longhi, D. Gatti, and G. D. Valle, Robust light transport in non-Hermitian photonic lattices, Sci. Rep. **5**, 13376 (2015).

[15] W. Chen, Ş. Kaya Özdemir, G. Zhao, J. Wiersig, and L. Yang, Exceptional points enhance sensing in an optical microcavity, Nature (London) **548**, 192 (2017).

[16] L. Xiao, X. Zhan, Z. H. Bian, K. K. Wang, X. Zhang, X. P. Wang, J. Li, K. Mochizuki, D. Kim, N. Kawakami, W. Yi, H. Obuse, B. C. Sanders, and P. Xue, Observation of topological edge states in parity–time-symmetric quantum walks, Nat. Phys. **13**, 1117 (2017).

[17] B. Bahari, A. Ndao, F. Vallini, A. El Amili, Y. Fainman, and B. Kanté, Nonreciprocal lasing in topological cavities of arbitrary geometries, Science **358**, 636 (2017).

[18] M. A. Bandres, S. Wittek, G. Harari, M. Parto, J. Ren, M. Segev, D. N. Christodoulides, and M. Khajavikhan, Topological insulator laser: Experiments, Science **359**, eaar4005 (2018).

[19] K. Y. Bliokh, D. Leykam, M. Lein, and F. Nori, Topological non-Hermitian origin of surface Maxwell waves, Nat. Commun. **10**, 580 (2019).

[20] Ş. K. Özdemir, S. Rotter, F. Nori, and L. Yang, Parity–time symmetry and exceptional points in photonics, Nat. Mater. **18**, 783 (2019).

[21] Y. Ashida, Z. Gong, and M. Ueda, Non-Hermitian physics, Adv. Phys. **69**, 249 (2020).

[22] C. Leefmans, A. Dutt, J. Williams, L. Yuan, M. Parto, F. Nori, S. Fan, and A. Marandi, Topological dissipation in a time-multiplexed photonic resonator network, Nat. Phys. **18**, 442 (2022).

[23] I. I. Arkhipov, A. Miranowicz, F. Minganti, Ş. K. Özdemir, and F. Nori, Dynamically crossing diabolic points while encircling exceptional curves: A programmable symmetric-asymmetric multimode switch, Nat. Commun. **14**, 2076 (2023).

[24] Y. Singhal, E. Martello, S. Agrawal, T. Ozawa, H. Price, and B. Gadway, Measuring the adiabatic non-Hermitian Berry phase in feedback-coupled oscillators, Phys. Rev. Res. **5**, L032026 (2023).

[25] V. M. Martinez Alvarez, J. E. Barrios Vargas, and L. E. F. Foa Torres, Non-Hermitian robust edge states in one dimension: Anomalous localization and eigenspace condensation at exceptional points, Phys. Rev. B **97**, 121401(R) (2018).

[26] S. Yao and Z. Wang, Edge states and topological invariants of non-Hermitian systems, Phys. Rev. Lett. **121**, 086803 (2018).

[27] S. Yao, F. Song, and Z. Wang, Non-Hermitian Chern bands, Phys. Rev. Lett. **121**, 136802 (2018).

[28] F. Song, S. Yao, and Z. Wang, Non-Hermitian skin effect and chiral damping in open quantum systems, Phys. Rev. Lett. **123**, 170401 (2019).

[29] C. C. Wanjura, M. Brunelli, and A. Nunnenkamp, Topological framework for directional amplification in driven-dissipative cavity arrays, Nat. Commun. **11**, 3149 (2020).

[30] W.-T. Xue, Y.-M. Hu, F. Song, and Z. Wang, Non-Hermitian edge burst, Phys. Rev. Lett. **128**, 120401 (2022).

[31] L. Li, C. H. Lee, S. Mu, and J. Gong, Critical non-Hermitian skin effect, Nat. Commun. **11**, 1 (2020).

[32] C.-H. Liu, K. Zhang, Z. Yang, and S. Chen, Helical damping and dynamical critical skin effect in open quantum systems, Phys. Rev. Res. **2**, 043167 (2020).

[33] K. Yokomizo and S. Murakami, Scaling rule for the critical non-Hermitian skin effect, Phys. Rev. B **104**, 165117 (2021).

[34] C.-X. Guo, C.-H. Liu, X.-M. Zhao, Y. Liu, and S. Chen, Exact solution of non-Hermitian systems with generalized boundary conditions: Size-dependent boundary effect and fragility of the skin effect, Phys. Rev. Lett. **127**, 116801 (2021).

[35] X.-Q. Sun, P. Zhu, and T. L. Hughes, Geometric response and disclination-induced skin effects in non-Hermitian systems, Phys. Rev. Lett. **127**, 066401 (2021).

[36] K. Zhang, Z. Yang, and C. Fang, Universal non-Hermitian skin effect in two and higher dimensions, Nat. Commun. **13**, 1 (2022).

[37] Y. Li, C. Liang, C. Wang, C. Lu, and Y.-C. Liu, Gain-loss-induced hybrid skin-topological effect, Phys. Rev. Lett. **128**, 223903 (2022).

[38] W. Zhu and J. Gong, Hybrid skin-topological modes without asymmetric couplings, Phys. Rev. B **106**, 035425 (2022).

[39] C. Wu, A. Fan, and S.-D. Liang, Complex Berry curvature and complex energy band structures in non-Hermitian graphene model, AAPPS Bull. **32**, 39 (2022).
[40] M. Brandenbourger, X. Locsin, E. Lerner, and C. Coulais, Non-reciprocal robotic metamaterials, Nat. Commun. **10**, 4608 (2019).
[41] L. S. Palacios, S. Tchoumakov, M. Guix, I. Pagonabarraga, S. Sánchez, and A. G. Grushin, Guided accumulation of active particles by topological design of a second-order skin effect, Nat. Commun. **12**, 4691 (2021).
[42] W. Wang, M. Hu, X. Wang, G. Ma, and K. Ding, Experimental realization of geometry-dependent skin effect in a reciprocal two-dimensional lattice, Phys. Rev. Lett. **131**, 207201 (2023).
[43] T. Helbig, T. Hofmann, S. Imhof, M. Abdelghany, T. Kiessling, L. Molenkamp, C. Lee, A. Szameit, M. Greiter, and R. Thomale, Generalized bulk–boundary correspondence in non-Hermitian topolectrical circuits, Nat. Phys. **16**, 747 (2020).
[44] X. Zhang, Y. Tian, J.-H. Jiang, M.-H. Lu, and Y.-F. Chen, Observation of higher-order non-Hermitian skin effect, Nat. Commun. **12**, 5377 (2021).
[45] X. Zhang, B. Zhang, W. Zhao, and C. H. Lee, Observation of non-local impedance response in a passive electrical circuit, SciPost Phys. **16**, 002 (2024).
[46] S. Weidemann, M. Kremer, T. Helbig, T. Hofmann, A. Stegmaier, M. Greiter, R. Thomale, and A. Szameit, Topological funneling of light, Science **368**, 311 (2020).
[47] L. Xiao, T. Deng, K. Wang, G. Zhu, Z. Wang, W. Yi, and P. Xue, Non-Hermitian bulk–boundary correspondence in quantum dynamics, Nat. Phys. **16**, 761 (2020).
[48] Y. G. N. Liu, Y. Wei, O. Hemmatyar, G. G. Pyrialakos, P. S. Jung, D. N. Christodoulides, and M. Khajavikhan, Complex skin modes in non-Hermitian coupled laser arrays, Light: Sci. Appl. **11**, 336 (2022).
[49] C. R. Leefmans, M. Parto, J. Williams, G. H. Y. Li, A. Dutt, F. Nori, and A. Marandi, Topological temporally mode-locked laser, Nat. Phys. **20**, 852 (2024).
[50] W. Gou, T. Chen, D. Xie, T. Xiao, T.-S. Deng, B. Gadway, W. Yi, and B. Yan, Tunable nonreciprocal quantum transport through a dissipative Aharonov-Bohm ring in ultracold atoms, Phys. Rev. Lett. **124**, 070402 (2020).
[51] K. Yokomizo and S. Murakami, Non-Bloch band theory of non-Hermitian systems, Phys. Rev. Lett. **123**, 066404 (2019).
[52] K. Zhang, Z. Yang, and C. Fang, Correspondence between winding numbers and skin modes in non-Hermitian systems, Phys. Rev. Lett. **125**, 126402 (2020).
[53] H.-Y. Wang, F. Song, and Z. Wang, Amoeba formulation of non-Bloch band theory in arbitrary dimensions, Phys. Rev. X **14**, 021011 (2024).
[54] D. Leykam, K. Y. Bliokh, C. Huang, Y. D. Chong, and F. Nori, Edge modes, degeneracies, and topological numbers in non-Hermitian systems, Phys. Rev. Lett. **118**, 040401 (2017).
[55] H. Shen, B. Zhen, and L. Fu, Topological band theory for non-Hermitian Hamiltonians, Phys. Rev. Lett. **120**, 146402 (2018).
[56] Z. Gong, Y. Ashida, K. Kawabata, K. Takasan, S. Higashikawa, and M. Ueda, Topological phases of non-Hermitian systems, Phys. Rev. X **8**, 031079 (2018).
[57] K. Kawabata, S. Higashikawa, Z. Gong, Y. Ashida, and M. Ueda, Topological unification of time-reversal and particle-hole symmetries in non-Hermitian physics, Nat. Commun. **10**, 297 (2019).
[58] K. Kawabata, K. Shiozaki, M. Ueda, and M. Sato, Symmetry and topology in non-Hermitian physics, Phys. Rev. X **9**, 041015 (2019).
[59] H. Zhou and J. Y. Lee, Periodic table for topological bands with non-Hermitian symmetries, Phys. Rev. B **99**, 235112 (2019).
[60] D. S. Borgnia, A. J. Kruchkov, and R.-J. Slager, Non-Hermitian boundary modes and topology, Phys. Rev. Lett. **124**, 056802 (2020).
[61] K. Kawabata, T. Bessho, and M. Sato, Classification of exceptional points and non-Hermitian topological semimetals, Phys. Rev. Lett. **123**, 066405 (2019).
[62] Y. Xiong, Why does bulk boundary correspondence fail in some non-Hermitian topological models, J. Phys. Commun. **2**, 035043 (2018).
[63] C. H. Lee and R. Thomale, Anatomy of skin modes and topology in non-Hermitian systems, Phys. Rev. B **99**, 201103(R) (2019).
[64] T. Liu, Y.-R. Zhang, Q. Ai, Z. Gong, K. Kawabata, M. Ueda, and F. Nori, Second-order topological phases in non-Hermitian systems, Phys. Rev. Lett. **122**, 076801 (2019).
[65] C. H. Lee, L. Li, and J. Gong, Hybrid higher-order skin-topological modes in nonreciprocal systems, Phys. Rev. Lett. **123**, 016805 (2019).
[66] T. Liu, J. J. He, T. Yoshida, Z.-L. Xiang, and F. Nori, Non-Hermitian topological Mott insulators in one-dimensional fermionic superlattices, Phys. Rev. B **102**, 235151 (2020).
[67] H. Jiang, L.-J. Lang, C. Yang, S.-L. Zhu, and S. Chen, Interplay of non-Hermitian skin effects and Anderson localization in nonreciprocal quasiperiodic lattices, Phys. Rev. B **100**, 054301 (2019).
[68] X. Cai, Boundary-dependent self-dualities, winding numbers, and asymmetrical localization in non-Hermitian aperiodic one-dimensional models, Phys. Rev. B **103**, 014201 (2021).
[69] Y. Liu, Y. Wang, X.-J. Liu, Q. Zhou, and S. Chen, Exact mobility edges, $\mathcal{PT}$-symmetry breaking, and skin effect in one-dimensional non-Hermitian quasicrystals, Phys. Rev. B **103**, 014203 (2021).
[70] C. Yuce and H. Ramezani, Coexistence of extended and localized states in the one-dimensional non-Hermitian Anderson model, Phys. Rev. B **106**, 024202 (2022).
[71] S. Manna and B. Roy, Inner skin effects on non-Hermitian topological fractals, Commun. Phys. **6**, 10 (2023).
[72] A. Chakrabarty and S. Datta, Skin effect and dynamical delocalization in non-Hermitian quasicrystals with spin-orbit interaction, Phys. Rev. B **107**, 064305 (2023).
[73] L. Zhou, Non-Abelian generalization of non-Hermitian quasicrystals: $\mathcal{PT}$-symmetry breaking, localization, entanglement, and topological transitions, Phys. Rev. B **108**, 014202 (2023).
[74] J. Claes and T. L. Hughes, Skin effect and winding number in disordered non-Hermitian systems, Phys. Rev. B **103**, L140201 (2021).
[75] S. Longhi, Spectral deformations in non-Hermitian lattices with disorder and skin effect: A solvable model, Phys. Rev. B **103**, 144202 (2021).

[76] K.-M. Kim and M. J. Park, Disorder-driven phase transition in the second-order non-Hermitian skin effect, Phys. Rev. B **104**, L121101 (2021).

[77] B. A. Bhargava, I. C. Fulga, J. van den Brink, and A. G. Moghaddam, Non-Hermitian skin effect of dislocations and its topological origin, Phys. Rev. B **104**, L241402 (2021).

[78] R. Sarkar, S. S. Hegde, and A. Narayan, Interplay of disorder and point-gap topology: Chiral modes, localization, and non-Hermitian Anderson skin effect in one dimension, Phys. Rev. B **106**, 014207 (2022).

[79] K. Suthar, Y.-C. Wang, Y.-P. Huang, H. H. Jen, and J.-S. You, Non-Hermitian many-body localization with open boundaries, Phys. Rev. B **106**, 064208 (2022).

[80] H. Liu, M. Lu, Z.-Q. Zhang, and H. Jiang, Modified generalized Brillouin zone theory with on-site disorder, Phys. Rev. B **107**, 144204 (2023).

[81] W.-W. Jin, J. Liu, X. Wang, Y.-R. Zhang, X. Huang, X. Wei, W. Ju, T. Liu, Z. Yang, and F. Nori, Reentrant non-Hermitian skin effect induced by correlated disorder, arXiv:2311.03777 [Phys. Rev. Lett. (to be published)].

[82] L. Li, C. H. Lee, and J. Gong, Impurity induced scale-free localization, Commun. Phys. **4**, 42 (2021).

[83] P. Molignini, O. Arandes, and E. J. Bergholtz, Anomalous skin effects in disordered systems with a single non-Hermitian impurity, Phys. Rev. Res. **5**, 033058 (2023).

[84] C. Yuce and H. Ramezani, Non-Hermitian edge burst without skin localization, Phys. Rev. B **107**, L140302 (2023).

[85] F. Song, S. Yao, and Z. Wang, Non-Hermitian topological invariants in real space, Phys. Rev. Lett. **123**, 246801 (2019).

[86] K. Kawabata, M. Sato, and K. Shiozaki, Higher-order non-Hermitian skin effect, Phys. Rev. B **102**, 205118 (2020).

[87] N. Okuma, K. Kawabata, K. Shiozaki, and M. Sato, Topological origin of non-Hermitian skin effects, Phys. Rev. Lett. **124**, 086801 (2020).

[88] G. H. Wannier, Dynamics of band electrons in electric and magnetic fields, Rev. Mod. Phys. **34**, 645 (1962).

[89] T. Hartmann, F. Keck, H. Korsch, and S. Mossmann, Dynamics of Bloch oscillations, New J. Phys. **6**, 2 (2004).

[90] Q. Niu and F. Nori, Renormalization-group study of one-dimensional quasiperiodic systems, Phys. Rev. Lett. **57**, 2057 (1986).

[91] Q. Niu and F. Nori, Spectral splitting and wave-function scaling in quasicrystalline and hierarchical structures, Phys. Rev. B **42**, 10329 (1990).

[92] F. K. Kunst and V. Dwivedi, Non-Hermitian systems and topology: A transfer-matrix perspective, Phys. Rev. B **99**, 245116 (2019).

[93] M. Saha, B. K. Agarwalla, M. Kulkarni, and A. Purkayastha, Universal subdiffusive behavior at band edges from transfer matrix exceptional points, Phys. Rev. Lett. **130**, 187101 (2023).

[94] M. Saha, M. Kulkarni, and B. K. Agarwalla, Exceptional hypersurfaces of transfer matrices of finite-range lattice models and their consequences on quantum transport properties, Phys. Rev. B **108**, 075406 (2023).

[95] Here, we choose the principal branch of square root function in Eq. (15) to ensure that it is single-valued, by defining the angle of the argument of square root to be in $[0, 2\pi)$.

[96] T. Mori, Floquet states in open quantum systems, Annu. Rev. Condens. Matter Phys. **14**, 35 (2023).

[97] Y. Li, C. Lu, S. Zhang, and Y.-C. Liu, Loss-induced Floquet non-Hermitian skin effect, Phys. Rev. B **108**, L220301 (2023).

[98] M. Nakagawa, N. Kawakami, and M. Ueda, Non-Hermitian Kondo effect in ultracold alkaline-earth atoms, Phys. Rev. Lett. **121**, 203001 (2018).

[99] W. N. Faugno and T. Ozawa, Interaction-induced non-Hermitian topological phases from a dynamical gauge field, Phys. Rev. Lett. **129**, 180401 (2022).

[100] Y. Li, Z.-F. Cai, T. Liu, and F. Nori, Dissipation and interaction-controlled non-Hermitian skin effects, arXiv:2408.12451.

[101] T. Haga, M. Nakagawa, R. Hamazaki, and M. Ueda, Liouvillian skin effect: Slowing down of relaxation processes without gap closing, Phys. Rev. Lett. **127**, 070402 (2021).

[102] F. Yang, Q.-D. Jiang, and E. J. Bergholtz, Liouvillian skin effect in an exactly solvable model, Phys. Rev. Res. **4**, 023160 (2022).

[103] P.-C. Kuo, S.-L. Yang, N. Lambert, J.-D. Lin, Y.-T. Huang, F. Nori, and Y.-N. Chen, Non-Markovian skin effect, Phys. Rev. Res. **7**, L012068 (2025).

[104] S. Ma, H. Lin, and J. Pi, Imaginary gap-closed points and dynamics in a class of dissipative systems, Phys. Rev. B **109**, 214311 (2024).

[105] P. Wen, J. Pi, and G.-L. Long, Investigation of a non-Hermitian edge burst with time-dependent perturbation theory, Phys. Rev. A **109**, 022236 (2024).

[106] The convergence of eigenvalue perturbation series is a subtle problem in quantum mechanics, with many well-known cases exhibiting divergence. Nevertheless, our focus here is on a system with a finite chain length L and a correspondingly finite dimension of its Hilbert space. This finite dimensionality ensures the convergence of perturbation theory in this specific scenario [108]. Subsequently, we delve into an analysis of how the perturbed eigenvalues evolve as L increases.

[107] M. F. Triola, *Elementary Statistics Technology Update* (Pearson Education, Boston, 2012).

[108] B. Simon, Large orders and summability of eigenvalue perturbation theory: A mathematical overview, Int. J. Quantum Chem. **21**, 3 (1982).